First-principles and thermodynamics comparison of compositionally-tuned delafossites: Cation release from the (001) surface of complex metal oxides

Joseph W. Bennett[1], Diamond Jones[1], Blake G. Hudson[1], Joshua Melendez-Rivera[2], Robert J. Hamers[3] and Sara E. Mason[1]**

1: Department of Chemistry
University of Iowa, Iowa City, Iowa 52242;
Department of Chemistry
The University of Puerto Rico at Cayey, P. O. Box 372230, Cayey, PR 00737-2230, USA
3: Department of Chemistry
University of Wisconsin-Madison, Madison, WI 53706

E-mail: sara-mason@uiowa.edu

Abstract

Nanoscale complex metal oxides have transformed how technology is used around the world. A ubiquitous example is the class of electroreactive cathodes used in Li-ion batteries, found in portable electronics and electric cars. Lack of recyling infrasructure and financial drivers contribute to improper disposal, and ultimate introduction of these materials into the environment. Outside of sealed operational conditions, it has been demonstrated that complex metal oxides can transform in the environment, and cause negative biological impact through leaching of cations into aqueous phases. Using a combined DFT + Thermodynamics analysis, insights into the mechanism and driving forces of cation release can be studied at the molecular-level. Here, we describe design principles that can be drawn from previous collaborative research on complex metal oxide dissoltuion of the $Li(Ni_yMn_zCo_{1-y-z})O_2$ family of materials, and go on to posit ternary complex metal oxides in the delafossite structure type with controlled release behavior. Using equistoichiometric formulations, we use DFT + Thermodynamics to model cation release. The trends are discussed in terms of lattice stability, solution chemistry/solubility limits, and electronic/magnetic properties. Inercalation voltages are calculated and discussed as a predictive metric for potential functionality of the model materials.

Introduction

Manufacturing of nanoscale complex metal oxides (CMOs) is on the rise, concurrent with their use in mobile devices and renewable energy applications.[1–3] A key example is the delafossite structure type, which has found increased use as one of the prominent families of intercalation materials used in lithium-ion batteries (LIBs). The delafossite CMOs used in LIBs are the electroactive components of the cathode,[4–7] and the prototypical example is $LiCoO_2$ (LCO). To decrease the cost and increase the performance of materials based on LCO, compositional tuning has led to $Li(Ni_{1/3}Mn_{1/3}Co_{1/3})O_2$ (NMC) materials,[8–11] and other variants

2

such as high-Ni NMC compositions, which are readily synthesizable and demonstrate both high voltage in operation and enhanced cycle stability.[12,13] While compositionally tuned variants of LCO and NMC have been advantageous because of their improved properties and ease of manufacturing, they also contain transition metals whose release has been shown to be potentially toxic to a wide variety of organisms.[14–21] The proposed mechanisms of negative biological impact include both a) an increased concentration of potentially toxic cations in solution via incongruent CMO surface release of Ni and Co[14] and b) oxidative stress caused by the generation of reactive oxygen species (ROS) *in situ.*[22]

To better understand the thermodynamics of surface transformations that enable cation release, we evoke a DFT+ solvent ion model.[7,23] Our test cases included compositionally tuned variants of NMC (equistoichiometric and Mn-rich NMC) that contain multiple cations whose oxidation states depended upon atomistic composition, surface termination, and the formation of vacancies. We were able to combine DFT-computed (001) surface vacancy energies and experimentally determined aqueous thermodynamics to show that metal release depends upon oxidation state and chemical environment of the cations, via surface terminations and neighboring cations. More importantly we were able to agree with trends in experimental release (Li > Ni > Co > Mn) and go on to inform experiments using Ni-rich NMC compositions (*Buchman et al.*, under review).

Briefly, the nominal valence of the cations in NMC are Ni^{2+}, Co^{3+}, and Mn^{4+} and the aqueous stable valences of these cations are Ni^{2+}, Co^{2+}, and Mn^{2+}. This means that releasing a Co or Mn from the (001) surface of NMC would require additional reduction steps to the 2+ state, but the release of Ni^{2+} from NMC would not. Both experiment and our model agree that higher oxidation state metals, such as Mn^{4+}, were more resistant to surface release. We then found that enriching NMC with Mn created a population of Mn^{2+} in the solid state, to maintain charge balance, and that this was more likely to be released than Mn^{4+}. The opposite was true of Ni enriched NMC; more Ni^{3+} and Ni^{4+} were formed in the solid state to balance charge, and were less likely to be released from the surface than Ni^{2+}. The DFT

3

+ solvent ion model was able to show how adjusting the composition of the NMC delafossite structure allowed for controlled release of metals from the surface of CMOs via an analysis that coupled the thermodynamics of vacancy formations to an understanding of oxidation states and chemical environment.

One of our ultimate goals is to apply the understanding obtained from the computational modeling to the rational design of CMOs that mitigate the release of potentially toxic surface cations in aqueous media, specifically by changing the chemical environment of the cations in a CMO via neighboring atoms. One route would be to choose cations that, at circumneutral or slightly acidic pH, are thermodynamically not favored to be released. Another route would be to encourage the release of cations that are more innocuous to a wide range of organisms. If any of the compositions are to be adopted industry-wide, then they must also be cost-effective replacements for elements such as Ni and Co, and demonstrate a comparable operating voltage. Here we present a survey of the properties of bulk and surface CMO compositions that include Ti, V, Mn, Fe, Co, Ni, Al. This set spans the elements of the $3d$-block and includes Al. Each of these metals are less expensive than Co, can be found in octahedral coordination, and are known to form at least one stable cationic oxidation state between $+2$ and $+4$.

We use the DFT + solvent ion model as a screening mechanism to better couple atomistic information about oxidation and spin states to an understanding of the effects of compositional tuning on the thermodynamics of metal release from the (001) surface. We report on the bulk and surface structures, including the effects of de-lithiation and surface metal release to gauge the series of redox events that may take place while under standard operating conditions or exposed to aqueous environments. We create equistoichiometric compositions of general chemical formula $Li(A_{1/3}B_{1/3}C_{1/3})O_2$ such as $Li(Ni_{1/3}Mn_{1/3}Fe_{1/3})O_2$ (NMF) and $Li(Fe_{1/3}Ti_{1/3}V_{1/3})O_2$ (FTV) to compare to LCO and NMC. The sets of materials presented here are referred to as the generic 333-ABC delafossites, and Figure 1 shows how one could change composition from LCO to NMC to FMA to create comparable 333-ABC composi-

4

tions. NMC is created from LCO by replacing 1/3 of the Co with Ni and 1/3 of the Co with Mn; FMA is created from NMC by replacing Ni with Fe and Co with Al.

There has been a large effort to replace the toxic and flammable organic electrolytes in LIB to those that are aqueous since 1994.[24] LIBs with aqueous electrolytes, aqueous lithium-ion batteries (ALIBs), have the potential to be safer with cheaper production costs, and up to two orders of magnitude higher ionic conductivity than their non-aqueous counterparts.[25] Unfortunately, many of these initial batteries have low cyclability due to instability of the compounds used for the electrodes.[26] More specifically, when lithium intercalation compounds such as $LiMn_2O_4$, LCO, and NMC, were used as the cathode, it was found that the pH of the electrolyte was important for the stability of the cathode.[27] Therefore, the stability of these materials in aqueous environments, i.e. solubility[28] must be considered for use in the new frontier of high energy storage. Here we suggest cathode materials that have limited solubility depending on the pH range.

The complete set of 333-ABC is as follows: $Li(Co_{1/3}Fe_{1/3}Al_{1/3})O_2$ (CFA), $Li(Ni_{1/3}Mn_{1/3}Co_{1/3})O_2$ (NMC), $Li(Ni_{1/3}Mn_{1/3}Al_{1/3})O_2$ (NMA), $Li(Ni_{1/3}Mn_{1/3}Fe_{1/3})O_2$ (NMF), $Li(Ni_{1/3}V_{1/3}Fe_{1/3})O_2$ (NVF), $Li(Fe_{1/3}Mn_{1/3}Al_{1/3})O_2$ (FMA), $Li(V_{1/3}Mn_{1/3}Al_{1/3})O_2$ (VMA), $Li(Fe_{1/3}Ti_{1/3}Al_{1/3})O_2$ (FTA), $Li(Fe_{1/3}Ti_{1/3}V_{1/3})O_2$ (FTV), and $Li(V_{1/3}Ti_{1/3}Al_{1/3})O_2$ (VTA). This set is sufficient to allow for insights into the thermodynamics of surface release of early transition metals such as Ti and V, to compare to previous work on the surface dissolution of later transition metals such as Co and Ni.[7,29,30] Moreover, metals such as Ti, V, and Al are known to form stable oxides at pH values below 7, implying that surface release of these metals might be minimal at specific pH values, if they occur at all, and that they might impart additional lattice stabilization to prevent surface metal release.

After analyzing trends in (001) surface release we go on to present a set of design rules for the rational redesign of CMOs through compositional tuning, with an eye towards potentially reduced adverse interactions at the nano-bio interface and increased sustainability. We go on to suggest how the vacancy structures resulting from cation release could be used to create
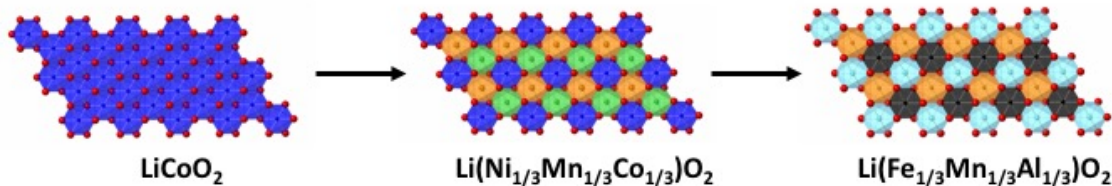
Figure 1: From left to right are top-down depictions of $LiCoO_2$ (LCO), $Li(Ni_{1/3}Mn_{1/3}Co_{1/3})O_2$ (NMC), and $Li(Fe_{1/3}Mn_{1/3}Al_{1/3})O_2$ (FMA) layers, which are formed using successive equistoichiometric metal substitutions of the delafossite structure type. Co, Ni, and Mn are depicted as dark blue, green, and orange, respectively. Fe and Al are depicted as light blue and black, respectively. All red spheres are O.

more sustainable catalytic systems for environmental/remediation applications.

Materials and Methods

All bulk and surface calculations employ periodic DFT calculations,[31,32] and are carried out using using Quantum Espresso, an open source software package.[33] Calculations are performed at the GGA level[34] using the PBE-GGA exchange correlation functional. The level of DFT that is used here has been shown to underestimate the bandgaps, but has been shown previously to capture the qualitative trends we are studying.[35,36] All atoms are represented as ultrasoft GBRV-type pseudopotentials,[37,38] and all calculations use a plane-wave cutoff of 40 Ry for the wavefunction and 320 Ry for the charge density. The convergence criterion for self-consistent relaxations was a maximum residual force of 5 meV/Å per atom, and all atoms are allowed to relax during structural optimizations. The bulk cells are based on a $[\sqrt{3} \times \sqrt{3}]R30^o$ rotated modification of the delafossite unit cell, to contain three octahedrally bound cations sites in a perfectly alternating manner. This modification also requires that the bulk cells be six layers, two lithium channels and four metal oxide layers, in the vertical direction, to maintain inversion symmetry critical to surface slab modeling,[39] which is doubled compared to the delafossite unit cell. Owing to the relatively large cell size, all bulk calculations are found to be converged with respect to energy and force using a 6×6×3 k-point grid.[40]

Previous experimental characterization showed that as-synthesized delafossite nanosheets have at least seven O-M-O layers,[14] which would be computationally expensive for the supercell compositions that we are investigating. Therefore, the delafossite surface slabs used here include four total metal oxide layers (O-M-O), like the NMC surfaces in Refs.,[7,23] of which the two interior and two exterior layers are related by inversion symmetry. The (001) surfaces presented here are based on a $[\sqrt{3} \times \sqrt{3}]R30^o$ rotated modification of the LiCoO$_2$ unit cell, where all Li$(A_{1/3}B_{1/3}C_{1/3})$O$_2$ surfaces have in plane dimensions of $2\sqrt{3} \times \sqrt{3}$ and at least 15 Å of vacuum separating each surface slab. This results in 6 total M per surface, where removal of 1 M results in a 16.67% surface vacancy density. All $2\sqrt{3} \times \sqrt{3}$ surface relaxations, including defect structures for modeling metal release, use a $3\times6\times1$ k-point grid.

We model the process of surface metal release (as the initial step of dissolution) step-wise. The first step is exchange of surface Li with H, and the second step is removing an H, O, and metal (M) from the (001) surface. We assume that the removal of any M-OH species results in a delocalization of electrons, since operation of Li-ion batteries relies upon the oxidation/reduction response of redox active M in the cathode. To compute the change in free energy associated with metal release, ΔG_{tot}, a DFT + solvent ion method[7,23,41,42] based on Hess's Law is employed. In the DFT + solvent ion method, ΔG_{tot} is partitioned between the computed energies of the reactants and products (used in ΔG_1) and experimental data (used in ΔG_2). Zero-point energy (ZPE) correction terms are added to the DFT total energies of NMC slabs to obtain $\Delta G_1 = E_{\text{products}}$ - $E_{\text{reactants}}$ + ZPE, as described in Ref.[7] and in the style on Ref.[41] Based on the previous work, we assume that the minimum energy pathway of release involves removal of an M-OH unit. The total energies of M, O, and H released from the surface are for the atoms in their standard state, which implies that ΔG_1 can be used as a term that gauges relative lattice stability for the removal of an isolated M-OH unit per surface slab.

The second model term, ΔG_2, is based on the Nernst equation. $\Delta G_2 = \Delta G^0_{\text{SHE}}$ - $n_e e U_{\text{SHE}}$ - 2.303n_{H^+}kT pH + kT ln a(H$_x$AO$_y^{z-}$), where ΔG^0_{SHE} is the change in free energy of the

aqueous cation/anion relative to the standard state, referenced to the standard hydrogen electrode (SHE). eU_{SHE} is the applied potential, relative to the SHE, and $\mathrm{H}_x\mathrm{AO}_y^{z-}$ are the concentrations of the released aqueous ions. Here we assume that no external potential is applied ($eU_{\mathrm{SHE}}=0$) and that ion concentrations are 1×10^{-6}M, an order of magnitude in line with measurements of released cations reported in experiment.[14,16] n_e and n_{H^+} are the number of electrons and protons involved in the chemical reactions required for surface release. They are zero for the aqueous species in the pH region of 1 to 7 investigated here, except for VO^{2+}, where n_e and n_{H^+} are 4 and 2, respectively, from the equation $\mathrm{V} + \mathrm{H}_2\mathrm{O} \rightarrow \mathrm{VO}^{2+} + 2\mathrm{H}^+ + 4e\text{-}$. Values of $\Delta G^0_{\mathrm{SHE}}$ for each cation are obtained from Ref.[43] and are tabulated in units of eV in Table 1. Also found in Table 1 are the speciation of Al, Ti, V, Mn, Fe, Co, Ni for pH values 1-7 from DFT-computed Pourbaix diagrams.[44]

Table 1: For each element in the first column, both the stable aqueous and solid species between pH values 1 to 7, and the pH range for which they will occur, are reported. The $\Delta G^0_{\mathrm{SHE}}$ of each aqueous species is also tabulated, given in units of eV.

element	cation	pH	$\Delta G^0_{\mathrm{SHE}}$ (eV)	solid	pH
Al	$\mathrm{Al}^{3+}(\mathrm{aq})$	1-5	-5.027	$\mathrm{Al}_2\mathrm{O}_3(\mathrm{s})$	5-7
Ti	-	-	-	$\mathrm{TiO}_2(\mathrm{s})$	1-7
V	$\mathrm{VO}^{2+}(\mathrm{aq})$	1-5	-6.084	$\mathrm{VO}_2(\mathrm{s})$	5-7
Mn	$\mathrm{Mn}^{2+}(\mathrm{aq})$	1-7	-2.363	-	-
Fe	$\mathrm{Fe}^{2+}(\mathrm{aq})$	1-6	-0.818	$\mathrm{Fe}_2\mathrm{O}_3(\mathrm{s})$	6-7
Co	$\mathrm{Co}^{2+}(\mathrm{aq})$	1-7	-0.563	-	-
Ni	$\mathrm{Ni}^{2+}(\mathrm{aq})$	1-7	-0.472	-	-

Results

Bulk structures

The bulk cell shown in Figure 2 is a $(\sqrt{3}\times\sqrt{3})\mathrm{R}30^o\times 2$ modification of a hexagonal delafossite primitive cell as described in previous studies.[45,46] The bulk $\mathrm{Li}(A_{1/3}B_{1/3}C_{1/3})\mathrm{O}_2$ (333-ABC) cell contains four metal oxide layers (O-M-O). To create 333-ABC delafossite structure types,
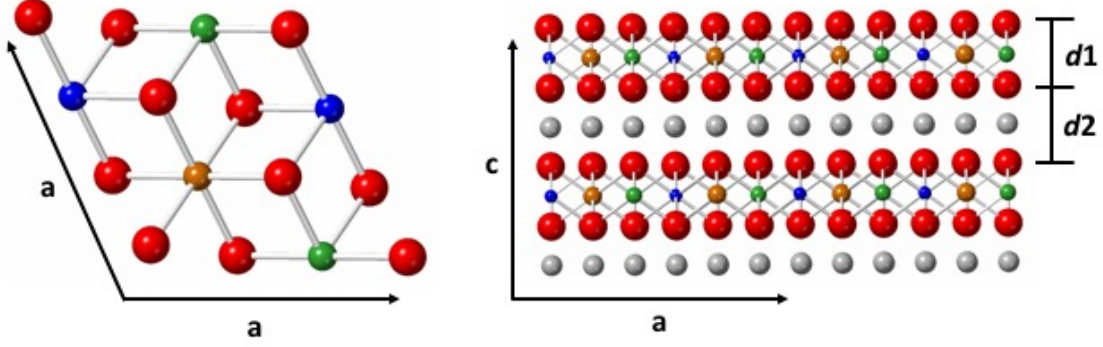
Figure 2: (Left) Top view of a metal oxide layer of the $\sqrt{3} \times \sqrt{3}$ R30^0 bulk 333-ABC cell. (Right) Side view of the layer ordering in bulk 333-ABC, with layer spacings $d1$ (O-M-O) and $d2$ (O-Li-O). The M are depicted as follows: Co is dark blue, Ni is green, and Mn is orange. Li is depicted as gray and O is red.

all equistoichiometric compositions contain metal cations bound in octahedra in a perfectly alternating manner that adheres to the trigonal symmetries of the delafossite structure type. The metal ordering in each layer is shown on the left hand-side of Figure 2.The right hand-side shows a condensed version, 2 O-M-O and one lithium channel, of the vertical direction is shown on the right-hand side of Figure 2. Distances $d1$ and $d2$ describe the vertical O-M-O and O-Li-O distances, respectively, and are shown for each fully relaxed bulk 333-ABC in Table 2. The range of $d1$ is 2.07 (CFA) to 2.30 Å (FTV) and the range of $d2$ is 2.61 (NVF) to 2.67 Å (multiple); the vertical O-Li-O distance is less sensitive to metal substitution in our 11 compositions than the O-M-O distances. The differences in lattice constant a, ≈ 0.1 Å, is also less sensitive to compositional tuning than lattice constant c, where the change in c going from NMC to FTV is ≈ 0.5 Å. The third to last column in Table 2 is the band gap (E_{gap}) of the bulk materials. All 333-ABC combinations are insulators, where the largest values of E_{gap} are for the compositions NMC (1.20 eV) and NMA (1.16 eV), and the smallest values of E_{gap} are found in the combinations NVF (0.18 eV) and FTV (0.17 eV). We also report, in Table 2, theoretical enthalpies of formation, per formula unit (E_f), for all of the CMOs and found them to all be favorable and within a ≈ 28 eV range. Details of the enthalpy calculations can be found in section S1 in the SI.

9

Table 2: Lattice parameters a and c of the bulk delafossite cells, and next are the corresponding interlayer spacings $d1$ and $d2$ (all in units of Å. The band gap (E_{gap}) is given, in units of eV. Finally, the average voltage between the fully lithiated and delithiated bulk for each CMO.

	a (Å)	c (Å)	$d1$ (Å)	$d2$ (Å)	E_{gap} (eV)	E_f (eV)	Voltage (V)
LCO	2.848	14.032	2.03	2.64	1.12	-55.56	3.56
CFA	2.840	14.233	2.07	2.67	0.74	-38.93	3.38
NMC	2.883	14.232	2.12	2.62	1.20	-53.48	3.17
NMA	2.879	14.327	2.12	2.65	1.16	-39.21	3.60
NMF	2.922	14.442	2.20	2.62	0.58	-51.13	3.01
NVF	2.918	14.552	2.24	2.61	0.18	-47.89	2.89
FMA	2.836	14.378	2.13	2.67	0.35	-34.66	3.05
VMA	2.856	14.552	2.18	2.67	0.28	-29.51	2.68
FTA	2.931	14.582	2.19	2.67	1.04	-40.33	3.02
FTV	2.934	14.771	2.30	2.62	0.17	-36.95	2.56
VTA	2.910	14.614	2.20	2.67	0.44	-25.03	2.47

Using the *ab initio* method of computing the intercalation voltage, V, we can assess the functionality of our proposed CMOs. The calculation of V requires the total energy of the CMOs with varying lithium content. For comparable systems, Ceder et al. measures the voltage for bulk NMC structures with 3 and 6 lithium atoms and finds that NMC should have a voltage of 3.0-4.5 V over the delithiation process.[47] In this work it is pointed out that finding the minimum energy structure for each level of delithiation step can be computationally taxing due the number of possible configurations. Specifically, for n Li atoms, a total of 2^n unique configurations can be formed in the bulk cell. To sidestep the issue of configurations, which would not provide chemical insights germane to the rational design of CMOs with controlled release profiles, we compare the fully lithiated structure, $\text{Li}_{1.00}$, and the fully delithiated structure, $\text{Li}_{0.00}$, to get a predicted voltage for each of our materials using Equation 1. Our predicted voltages can be found in the last column of Table 2. To more completely map out the voltage profiles of the 333-ABC series would require smaller step sizes of successive Li removal.

$$V = \frac{E[Li_{0.00}(A_{1/3}B_{1/3}C_{1/3})O_2] + E(Li_{metal}) * (Li_{1.00} - Li_{0.00}) - E[Li_{1.00}(A_{1/3}B_{1/3}C_{1/3})O_2]}{(Li_{1.00} - Li_{0.00}) * F}$$

(1)

As reported in Table 2, we observe that V increases with substitution of metals with Al, as shown by the difference in voltage for NMF (3.01 V) and NMA (3.60 V), and FTV (4.56 V) and FTA (3.02 V). This is a significant increase of at least 20%, which agrees with previous research.[48,49] We return to this trend, and offer chemical insight into its origin, after completing electronic structure analysis.

Effects of Compositional Tuning on Surface Properties

State-by-state, atom-by-atom projected density of states (PDOS) analysis was carried out for the surface structures of all CMO compositions. PDOS analysis offers a chemically intuitive description of the DFT charge density, and is used here to quantify the filling of specific orbitals for the transition metals in material, which are then used to assign the oxidation states of the metal sites in the model surfaces. In general, the oxidation states of the metals in the pristine surfaces (prior to the introduction of defects) are consistent across all formulations, with Co and Al always being 3^+, Ti and Mn being 4^+ and Ni always being 2^+. Fe and V are the only metals with varied oxidation states from 2^+ to 3^+. The band gap (E_{gap}) was tabulated from the electronic band structure for the bulk and surface, with the surfaces having smaller values of E_{gap}, relative to bulk counterparts. The largest variation in E_{gap} was found in NMC, with a difference of 0.8012 eV and the smallest was FTA and FTV with a 0.03 eV difference. We find that the values of E_{gap} for surfaces are not drastically different from those of the bulk solid solutions.

The PDOS analysis provides insight into the aforementioned trends in V, specifically that substitution of a transition metal with Al in the C site always increases the intercalation voltage. As discussed by Aydinal et $al.$, delithiation is accompanied by donation of electron

densitry to the oxygen 2p states in the lattice. As shown in Figure 3, when the C site is occupied by a transition metal, the oxygen 2p states are more delocalized, and show greater intensity just below the Fermi level. When Al is substituted, the PDOS of the oxygen 2p states show diminished intensity and less spread in energy near the Fermi level, which would impede the ability of these states to accept electron density and thereby driving up the value of V.

Table 3: Calculated oxidation states of surface metals A, B, and C in the 333-ABC delafossites. The final column, E_{gap}, is the electronic band gap reported in units of eV.

	A	B	C	E_{gap} (eV)
CFA	Co^{3+}	Fe^{3+}	Al^{3+}	0.02
NMC	Ni^{2+}	Mn^{4+}	Co^{3+}	0.40
NMA	Ni^{2+}	Mn^{4+}	Al^{3+}	0.85
NMF	Ni^{2+}	Mn^{4+}	Fe^{3+}	0.05
NVF	Ni^{2+}	V^{4+}	Fe^{3+}	-
FMA	Fe^{2+}	Mn^{4+}	Al^{3+}	0.17
VMA	V^{3+}	Mn^{3+}	Al^3	0.21
FTA	Fe^{2+}	Ti^{4+}	Al^{3+}	1.07
FTV	Fe^{2+}	Ti^{4+}	V^{3+}	0.14
VTA	V^{2+}	Ti^{4+}	Al^{3+}	0.37

Thermodynamic Comparisons

We tabulate all values of ΔG_1, ΔG_2 (at pH 6), and ΔG_{tot} for the metals in the 11 333-ABC compositions in Table 4, to compare to the LCO parent structure where the ΔG_1 to release Co-OH from the (001) surface is 9.40 eV, and ΔG_2 (at pH 6) for Co is -9.68 eV. This yields an overall ΔG = -0.28 eV for Co release from LCO at pH 6.

At pH 6, the preferred speciation of Al, Ti, V, and Fe are $Al_2O_3(s)$, $TiO_2(s)$, $VO_2(s)$, and $Fe_2O_3(s)$; ΔG_2 values for these species are undefined, so overall ΔG_{tot} is also undefined. Release of these species at pH 6 is not predicted to occur.

Figure 3 shows that substitution of Al with Fe, as in going from NMA to NMF, causes

Table 4: Thermodynamics of release at pH 6 for each cation of the 333-ABC compositions. The DFT-computed ΔG_1 values are added to ΔG_2 values to obtain ΔG_{rel} values for each cation A, B, and C. All values are reported in units of eV, and a - indicates than the thermodynamically preferred species is a solid phase.

	A	ΔG_1	ΔG_2	ΔG_{tot}	B	ΔG_1	ΔG_2	ΔG_{tot}	C	ΔG_1	ΔG_2	ΔG_{tot}
LCO	Co	9.40	-9.68	-0.28	-	-	-	-	-	-	-	-
CFA	Co	9.76	-9.68	+0.08	Fe	8.91	-	-	Al	13.28	-	-
NMC	Ni	8.36	-9.59	-1.23	Mn	12.46	-11.48	+0.98	Co	9.72	-9.68	+0.04
NMA	Ni	8.27	-9.59	-1.32	Mn	13.45	-11.48	+1.97	Al	14.42	-	-
NMF	Ni	7.35	-9.59	-2.24	Mn	11.25	-11.48	-0.23	Fe	9.78	-	-
NVF	Ni	6.07	-9.59	-3.52	V	12.00	-	-	Fe	8.15	-	-
FMA	Fe	7.31	-	-	Mn	9.68	-11.48	-1.80	Al	11.54	-	-
VMA	V	9.89	-	-	Mn	9.67	-11.48	-1.81	Al	11.10	-	-
FTA	Fe	7.72	-	-	Ti	14.39	-	-	Al	12.82	-	-
FTV	Fe	8.23	-	-	Ti	13.25	-	-	V	10.22	-	-
VTA	V	9.27	-	-	Ti	12.55	-	-	Al	11.68	-	-

Mn surface vacancy energy to decrease by ≈ 2 eV, such that Mn release from NMF is thermodynamically preferred relative to release from NMA or even NMC. Another example of significant change in ΔG_{tot} for Mn is seem in NMA and VMA: Substitution of Ni with V decreases ΔG_1 of Mn and Al by ≈ 4 and 3 eV, respectively. Focusing on Mn/Al compositions, replacing Fe with V going from FMA to VMA the ΔG_1 values of Mn are similar, and ΔG_1 values of Al change only by 0.4 eV. If Ni is present, as in NMA, ΔG_1 values of Mn and Al are both larger by ≈ 4 eV.

Comparing trends in values of ΔG_{tot} presented in Table 4, we find that compositional tuning has a significant effect on surface vacancy formation and subsequent metal release. Going from NMC to NMA to NMF to NVF the vacancy formation energy of Ni-OH successively decreases. Ni release is predicted to be favorable for all three 333-ABC combinations, and surface vacancy formation is most likely from NVF. When comparing the ΔG_1 of Ni for these four CMO's, where the higher values of ΔG_1 indicate higher lattice stability. Specifically, the combination of Mn/Al in NMA (8.27 eV) stabilizes Ni more-so than in NVF (6.07 eV). In this case, we explain the trends in surface energetics by the corresponding increased amount of unpaired spins on metal atoms in the surface.
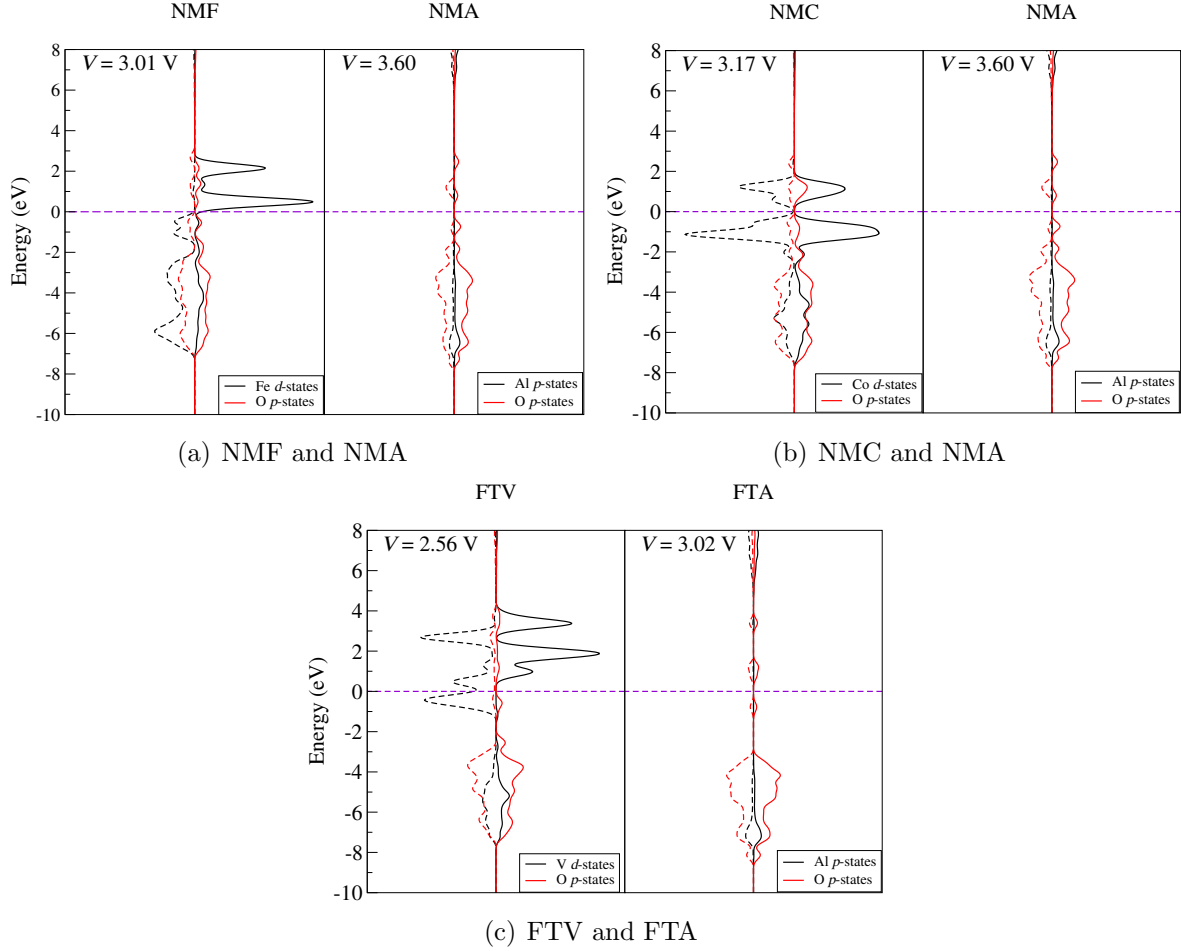
Figure 3: PDOS comparing the effects of substituting with Al in fully lithiated bulk structures. On the left of each plot is the valence electron desity of the transition metal (black) to be substituted with Al and the O states (red). Dashed lines represent spin down density, and solid lines are spin up. The fermi energy is set to zero and shown as a purple dashed line. (a) NMF and MVA (b) NMC and NMA (c) FTV and FTA.

In general, substituting Al for Co in NMC shows that Al-OH release is comparable to, or more energetically costly, than Co-OH removal. Substituting Ti for Mn (comparing FMA to FTA) shows that Ti-OH release is comparable to or more energetically costly than Mn-OH removal. Both Mn and Ti are consistently less prone to release than Co. It should also be noted that in the NWF and NVF compositions, it is thermodynamically more favorable to remove Fe than Co in NMC. This implies that Fe may be a beneficial substitution for Co in Mn and/or Ti-containing solid solutions.

Analysis of the surface energetics suggests that the absolute value of the total spin can

Table 5: ΔG_1 at pH 6 when the A-site metal is Ni and V and the composition is varied stepwise. Spin values for each cation A, B, and C are obtained from the PDOS analysis in the SI. All ΔG values are reported in units of eV. The final column is the absolute value of the total spin.

CMO	$\Delta G_1(A)$	TM_A spin	TM_B spin	TM_C spin	$|TotalSpin|$
NMC	8.36	+1.0	-1.5	0.0	0.5
NMA	8.27	+1.0	-1.5	0.0	0.5
NMF	7.35	+1.0	-1.5	+2.5	2.0
NVF	6.07	+1.0	-0.5	+2.5	3.0
VMA	9.89	+1.5	-1.5	0.0	0.0
VTA	9.27	+1.5	0.0	0.0	1.5

Table 6: ΔG_1 at pH 6 of where the A-site metal is Fe. Spin values for each of the metals was obtained from the PDOS analysis in the SI. The final column is the absolute value of the total spin.

CMO	$\Delta G_1(A)$	TM_A spin	TM_B spin	TM_C spin	$|TotalSpin|$
FTV	8.23	0.0	0.0	+1.0	1.0
FTA	7.72	0.0	0.0	0.0	0.0
FMA	7.31	0.0	-1.5	0.0	1.5

be used as a metric for predicting the lattice stability of the metal in the A-site. Following Table 5, going from NMC to NMA, we observe a small change (0.09 eV) of the ΔG_1 value where Co^{3+} (d^6) has no spin, is replaced with Al^{3+} (p^6) which also has no spin. In the next case, going from NMA to NMF, the Al is replaced with Fe^{3+} (d^5), high spin. This causes the absolute total spin of the entire system to increase by 1.5. With this increase in spin, we also observe the ΔG_1 for Ni decrease by 0.92 eV. As we increase the absolute spin through compositional tuning, we expect the stability of the A transition metal within the lattice to decrease, allowing for easier removal/dissolution. We also observe this trend for compositions where the A metal is Fe and V. We find an exception when the A-site metal is Fe, shown in Table 6 with FTA, the only CMO with no spin on any of the metals, where it has a lower absolute total spin than FMA, but a higher ΔG_1. We also compared the average spins for each metal for the bulk, surface and vaccancy structures shown in section S2 in the SI.

Across all compositions, Ni-OH release is the most thermodynamically favorable release, and is highly dependent upon chemical environment. The DFT-computed ΔG_1 of Ni-OH release decreases in order as NMC > NMA > NMF > NVF. The fact that it is thermodynamically favorable to release Ni when Fe is present with Mn or V suggests that this might be a route towards easier metal reclamation in aqueous media. The release trend per ion (taken as ΔG_1, in eV, averaged over all compositions that contain that cation) is: Ti-OH (13.40) > Al-OH (12.47) > Mn-OH (11.30) > V-OH (10.34) Co-OH (10.33) > Fe-OH (8.35) > Ni-OH (7.51). On average, the d^0 elements Ti(IV) and Al(III) are the least likely to be released, the mid-d-block elements Mn, V, Co, and Fe are more prone to surface release, and the late $3d$ metal Ni is thermodynamically preferred for release.

Conclusions

We use a DFT + solvent ion method to survey how compositional tuning of the delafossite structure would affect the surface metal release of CMOs in an aqueous environment, in line with recent efforts to transition from atomistic information obtained using DFT (in vacuum at 0 K) to operating/environmental conditions.[50–52] Our model finds that the surface metal release is highly dependent upon changes in composition; it is thermodynamically less favorable to create Ti or Al vacancies in the delafossite structure type than Fe or Ni. Elements such as V, Mn, and Fe were more likely to have a wide range of oxidation states than Ti, Ni, or Co, which were nominally Ti^{4+}, Ni^{2+}, and Co^{3+}. This implies that the mid $3d$-block elements will assume oxidation states dictated by the presence of early and late $3d$-block elements. The elements V and Ni were the first to change oxidation state with removal of a M-OH unit. These compositional changes alter the total spin of the material. When the total spin is increased, the dissolution of the metals becomes more favorable. We also tested to see if the functional properties of these materials were similar to NMC/LCO. We calculated te voltage, and found that the CMOs suggested are within the voltage range of

NMC/LCO. Replacing metals with Al will increase the voltage, suggesting a more functional battery.

The set of 333-ABC presented here yields insights into further developing technologies based on the CMO surface and its interface with aqueous media or the gas phase. Understanding the pH dependent behavior of CMO compositions is key to devising new strategies for cost-effective aqueous material processing,[53] increasing battery longevity,[54] and how CMOs might break down in the environment.[55] Recent work has pointed towards the use of waste CMOs as catalysts for the surface adsorption and oxidation of organic compounds.[56] The acid-assisted leaching of Li and Co cations to create surface vacancies in LCO was shown to adsorb and oxidize benzene, but the pH dependent thermodynamics of surface metal release and structures presented here could be used as a guide for design of more specific, tailorable catalytic systems.

Associated Content

The Supporting Information is available free of charge on the ACS Publications website at DOI:xxxx

Author Information

Corresponding Author: sara-mason@uiowa.edu

Notes: The authors declare no competing financial interest.

Acknowledgments

References

(1) Narins, T. P. The battery business: Lithium availability and the growth of the global electric car industry. *Extractive Industries and Society* **2017**, *4*, 321–328.

(2) Olivetti, E. A.; Ceder, G.; Gaustad, G. G.; Fu, X. Lithium-Ion Battery Supply Chain Considerations: Analysis of Potential Bottlenecks in Critical Metals. *Joule* **2017**, *1*, 229–243.

(3) Hamers, R. J. Nanomaterials and Global Sustainability. *Acc. Chem. Res.* **2017**, *50*, 633–637.

(4) Lu, J.; Chen, Z.; Ma, Z.; Pan, F.; Curtiss, L. A.; Amine, K. The role of nanotechnology in the development of battery materials for electric vehicles. *Nature Nanotech.* **2016**, *11*, 1031–1038.

(5) Ellingsen, L. A.-W.; Hung, C. R.; Majeau-Bettez, G.; Singh, B.; Chen, Z.; Whittingham, M. S.; Stromman, A. H. Nanotechnology for environmentally sustainable electromobility. *Nature Nanotech.* **2016**, *11*, 1039–1051.

(6) Larcher, D.; Tarascon, J.-M. Towards greener and more sustainable batteries for electrical energy storage. *Nature Chem.* **2014**, *7*, 19–29.

(7) Bennett, J. W.; Jones, D.; Huang, X.; Hamers, R. J.; Mason, S. E. Dissolution of complex metal oxides from first-principles and thermodynamics: Cation removal from the (001) surface of $Li(Ni_{1/3}Mn_{1/3}Co_{1/3})O2$. *Environ. Sci. Technol.* **2018**, *52*, 5792–5802.

(8) Hwang, B. J.; Tsai, Y. W.; Carlier, D.; Ceder, G. A Combined Computational/Experimental Study on $LiNi_{1/3}Co_{1/3}Mn_{1/3}O_2$. *Chem. Mater.* **2003**, *15*, 3676–3682.

(9) Sun, Y.-K.; Chen, Z.; Noh, H.-J.; Lee, D.-J.; Jung, H.-G.; Ren, Y.; Wang, S.; Yoon, C. S.; Myung, S.-T.; Amine, K. Nanostructured High-Energy Cathode Materials for Advanced Lithium Batteries. *Nature Mater.* **2012**, *11*, 942–947.

(10) Choi, N. S.; Chen, Z.; Freunberger, S. A.; Ji, X.; Sun, Y. K.; Amine, K.; Yushin, G.; Nazar, L. F.; Cho, J.; Bruce, P. G. Challenges Facing Lithium Batteries and ELectrical Double Layer Capacitors. *Angew. Chem. Int. Ed.* **2012**, *51*, 9994–10024.

(11) Rozier, P.; Tarascon, J.-M. Review-Li-Rich Layered Oxide Cathodes for Next-Generation Li-Ion Batteries: Chances and Challenges. *J. Electrochem. Soc.* **2015**, *162*, A2490–A2499.

(12) Zhao, W.; Zheng, J.; Zou, L.; Jia, H.; Liu, B.; Wang, H.; Engelhard, M. H.; Wang, C.; Xu, W.; Yang, Y.; Zhang, J.-G. High Voltage Operation of Ni-Rich NMC Cathodes Enabled by Stable Electrode/Electrolyte Interphases. *Adv. Energy Mater.* **2018**, *8*, 1800297.

(13) Yan, P.; Zheng, J.; Liu, J.; Wang, B.; Cheng, X.; Zhang, Y.; Sun, X.; Wang, C.; Zhang, J.-G. Tailoring Grain Boundary Structures and Chemistry of Ni-rich Layered

Cathodes for Enhanced Cycle Stability of Lithium-Ion Batteries. *Nature Energy* **2018**, *3*, 600–605.

(14) Hang, M. N.; Gunsolus, I. L.; Wayland, H.; Melby, E. S.; Mensch, A. C.; Hurley, K. R.; Pedersen, J. A.; Haynes, C. L.; Hamers, R. J. Impact of Nanoscale Lithium Nickel Manganese Cobalt Oxide (NMC) on the Bacterium Shewanella oneidensis MR-1. *Chem. Mater.* **2016**, 1092–1100.

(15) Dogangun, M.; Hang, M. N.; Machesky, J.; McGeachy, A. C.; Dalchand, N.; Hamers, R. J.; Geiger, F. M. Evidence for Considerable Metal Cation Concentrations from Lithium Intercalation Compounds in the Nano-Bio Interface Gap. *J. Phys. Chem. C.* **2017**, *121*, 27473–27482.

(16) Gunsolus, I. L.; Hang, M. N.; Hudson-Smith, N. V.; Buchman, J. T.; Bennett, J. W.; Conroy, D.; Mason, S. E.; Hamers, R. J.; Haynes, C. L. Influence of nickel manganese cobalt oxide nanoparticle composition on toxicity toward *Shewanella oneidensis* MR-1: redesigning for reduced biological impact. *Environ. Sci.: Nano.* **2017**, *4*, 636–646.

(17) Bozich, J.; Hang, M.; Hamers, R. J.; Klaper, R. Core chemistry influences the toxicity of multicomponent metal oxide nanomaterials, lithium nickel manganese cobalt oxide, and lithium cobalt oxide to *Daphnia magna*. *Environ. Toxicology and Chem.* **2017**, *36*, 2493–2502.

(18) Hang, M. N.; Hudson-Smith, N. V.; Clement, P. L.; Zhang, Y.; Wang, C.; Haynes, C. L.; Hamers, R. J. Influence of Nanoparticle Morphology on Ion Release and Biological Impact of Nickel Manganese Cobalt Oxide (NMC) Complex Oxide Nanomaterials. *ACS Appl. Nano Mater.* **2018**, *4*, 1721–1730.

(19) Feng, Z. V.; Miller, B. R.; Linn, T. G.; Pho, T.; Hoang, K.-N. L.; Hang, M. N.; Mitchell, S. L.; Hernandez, R. T.; Carlson, E. E.; Hamers, R. J. Biological impact of

nanoscale lithium intercalating complex metal oxides to model bacterium B. subtilis. *Environ. Sci.: Nano.* **2019**, *6*, 305–314.

(20) Cui, Y.; Melby, E. S.; Mensch, A. C.; Laudadio, E. D.; Hang, M. N.; Dohnalkova, A.; Hu, D.; Hamers, R. J.; Orr, G. Quantitative mapping of oxidative stress response to lithum cobalt oxide nanoparticles in single cells using multiplexed in situ gene expression analysis. *Nano Lett.* **2019**, *19*, 1990–1997.

(21) Niemuth, N. J.; Curtis, B. J.; Hang, M. N.; Gallagher, M. J.; Fairbrother, D. H.; Hamers, R. J.; Klaper, R. D. Next-generation complex metal oxide Nanomaterials negatively impact growth and development in the benthic invertebrate *chironomus riparius* upon settling. *Environ. Sci. Technol.* **2019**, *53*, 3860–3870.

(22) Qiu, T. A.; Gallagher, M. J.; Hudson-Smith, N. V.; Wu, J.; Krause, M. O. P.; Fortner, J. D.; Haynes, C. L. Research Highlights: Unveiling the Mechanisms Underlying Nanoparticle-Induced ROS Generation and Oxidative Stress. *Environ. Sci.: Nano* **2016**, *3*, 940–945.

(23) Bennett, J. W.; Jones, D. T.; Hamers, R. J.; Mason, S. E. First-principles and thermodynamics study of compositionally-tuned complex metal oxides: Cation release from the (001) surface of Mn-rich lithum nickel manganese cobalt oxide. *Inorg. Chem.* **2018**, *57*, 13300–13311.

(24) Li, W.; Dahn, J. R.; Wainwright, D. S. Rechargeable Lithium Batteries with Aqueous Electrolytes. *Science* **1994**, *264*, 1115–1118.

(25) Armand, M.; Tarascon, J. M. Building better batteries. *Nature* **2008**, *451*, 652–657.

(26) Bin, D.; Wen, Y.; Wang, Y.; Xia, Y. The development in aqueous lithium-ion batteries. *Journal of Energy Chem.* **2018**, *27*, 1521–1535.

(27) gang Wang, Y.; yan Luo, J.; xiao Wang, C.; yao Xia, Y. Hybrid Aqueous Energy Storage Cells Using Activated Carbon and Lithium-Ion Intercalated Compounds. *Elec. Soc. S.* **2005**, *153*, 1425–1431.

(28) Luo, J.-Y.; Cui, W.-J.; an Yong-Yao Xia, P. H. Raising the cycling stability of aqueous lithium-ion batteries by eliminating oxygen in the electrolyte. *Nat. Chem.* **2010**, *2*, 760–765.

(29) Buchman, J. T.; Evan A. Bennett, C. W.; AbbaspourTamijani, A.; Bennett, J. W.; Hudson, B. G.; Green, C. M.; Clement, P. L.; Zhi, B.; Henke, A.; Laudadio, E. D.; Mason, S. E.; Hamers, R. J.; Klaper, R. D.; Haynes, C. L.

(30) AbbaspourTamijani, A.; Bennett, J. W.; Jones, D. T.; Cartagena-Gonzalez, N.; Jones, Z. R.; Laudadio, E. D.; Hamers, R. J.; Santana, J. A.; Mason, S. E. 2019, DOI: `10.26434/chemrxiv.9764774.v1`.

(31) Hohenberg, P.; Kohn, W. Inhomogeneous Electron Gas. *Phys. Rev.* **1964**, *136*, B864–71.

(32) Kohn, W.; Sham, L. J. Self-Consistent Equations Including Exchange and Correlation Effects. *Phys. Rev.* **1965**, *140*, A1133–8.

(33) Giannozzi, P.; Baroni, S.; Bonini, N.; Calandra, M.; Car, R.; Cavazzoni, C.; Ceresoli, D.; Chiarotti, G. L.; Cococcioni, M.; Dabo, I.; et al., Quantum ESPRESSO: A Modular and Open-Source Software Project for Quantum Simulations of Materials. *J. Phys.:Condens. Matter* **2009**, *21*, 395502–20.

(34) Perdew, J. P.; Burke, K.; Ernzerhof, M. Generalized Gradient Approximation Made Simple. *Phys. Rev. Lett.* **1996**, *77*, 3865–8.

(35) Bennett, J. W.; Grinberg, I.; Rappe, A. M. New Highly Polar Semiconductor Ferro-

electrics through d^8 Cation-O Vacancy Substitution into PbTiO$_3$: A Theoretical Study. *JACS* **2008**, *130*, 17409–17412.

(36) Bennett, J. W.; Hudson, B. G.; Metz, I. K.; Spurgeon, S.; Cui, Q.; Mason, S. E. A systematic determination of Hubbard U using the GBRV ultrasoft pseudiopotential set. *Comp. Mat. Sci.* **2019**, *170*, 109137.

(37) Vanderbilt, D. Soft Self-Consistent Pseudopotentials in a Generalized Eigenvalue Formalism. *Phys. Rev. B Rapid Comm.* **1990**, *41*, 7892–5.

(38) Garrity, K. F.; Bennett, J. W.; Rabe, K. M.; Vanderbilt, D. Pseudopotentials for high-throughput DFT calculations. *Comp. Mater. Sci.* **2014**, *81*, 446–452.

(39) Corum, K. W.; Huang, X.; Bennett, J. W.; Mason, S. E. Systematic Density Functional Theory Study of the Structural and Electronic Properties of Constrained and Fully Relaxed (001) Surfaces of Alumina and Hematite. *Molecular Simulation* **2017**, *43*, 406–419.

(40) Monkhorst, H. J.; Pack, J. D. Special Points for Brillouin-Zone Integrations. *Phys. Rev. B* **1976**, *13*, 5188–5192.

(41) Rong, X.; Kolpak, A. M. Ab initio Approach for Prediction of Oxide Surface Structure, Stoichiometry, and Electrocatalytic Activity in Aqueous Solution. *Phys. Chem. Lett.* **2015**, *6*, 1785–1789.

(42) Rong, X.; Parolin, J.; Kolpak, A. M. A Fundamental Relationship between Reaction Mechanism and Stability in Metal Oxide Catalysts for Oxygen Evolution. *ACS Catal.* **2016**, *6*, 1153–1158.

(43) Wagman, D. D. E.; Halow, I.; Parker, V. B.; Bailey, S. M.; Schumm, R. H. Selected Values of Chemical Thermodynamic Properties. *National Bureau of Standards* **1971**,

(44) Persson, K. A.; Waldwick, B.; Lazic, P.; Ceder, G. Prediction of solid-aqueous equilibria: Scheme to combine first-principles calculations of solids with experimental aqueous states. *Phys. Rev. B.* **2012**, *85*, 235438.

(45) Huang, X.; Bennett, J. W.; Hang, M. N.; Laudadio, E. D.; Hamers, R. J.; Mason, S. E. *Ab initio* Atomistic Thermodynamics Study of the (001) Surface of $LiCoO_2$ in a Water Environment and Implications for Reactivity under Ambient Conditions. *J. Phys. Chem. C.* **2017**, *121*, 5069–5080.

(46) Koyama, Y.; Yabuuchi, N.; Tanaka, I.; Adachi, H.; Ohzuku, T. Solid State Chemistry and Electrochemistry of $LiCo_{1/3}Ni_{1/3}Mn_{1/3}O_2$ for Advanced Lithium-Ion Batteries. *J. ELectrochem. Soc.* **2004**, *151*, A1545–A1551.

(47) Hwang, B. J.; Tsai, Y. W.; Carlier, D.; Ceder, G. A Combined Computational/Experimental Study on $LiNi_{1/3}Co_{1/3}Mn_{1/3}O_2$. *Chem. Mater.* **2003**, *15*, 3676–3682.

(48) Aydinol, M. K.; Kohn, A. F.; Cedar, G.; Cho, K.; Joannopoulos, J. *AbInitio* study of Lithium intercalation in metal oxides and metal dichalcogenides. *Phys. Rev. B* **1997**, *56*, 1354–1365.

(49) Ceder, G.; Chiang, Y.-M.; Sadoway, D. R.; Aydinol, M. K.; Jang, Y.-I.; Huang, B. Identification of Cathode Materials for Lithium Batteries Guided by First-Principles Calculations. *Nature* **1998**, *392*, 694–696.

(50) Grajciar, L.; Heard, C. J.; Bondarenko, A. A.; Polynski, M. V.; Meeprasert, J.; Pidko, E. A.; Nachtigall, P. Towards Operando Computational Modeling in Heterogeneous Catalysis. *Chem. Soc. Rev.* **2018**, *47*, 8307–8348.

(51) Janet, J. P.; Liu, F.; Nandy, A.; Duan, C.; Yang, T.; Lin, S.; Kulik, H. J. Designing in the Face of Uncertainty: Exploiting Electronic Structure and Machine Learning Models for Discovery in Inorganic Chemistry. *Inorg. Chem.* **2019**,

(52) Vrieze, J. E. D.; Gunasooriya, G. T. K. K.; THybaut, J. W.; Saeys, M. Operando Computational Catalysis: Shape, Structure, and Coverage Under Reaction Conditions. *Current Opinion in Chem. Eng.* **2019**, *23*, 85–91.

(53) Bichon, M.; Sotta, D.; Dupre, N.; Vito, E. D.; Boulineau, A.; Porcher, W.; Lestriez, B. Study of Immersion of $LiNi_{0.5}Mn_{0.3}Co_{0.2}O_2$ Material in Water for Aqueous Processing of Positive Electrode for Li-Ion Batteries. *ACS Appl. Mater. Interfaces* **2019**, *11*, 18331–18341.

(54) Richards, W. D.; Miara, L. J.; Wang, Y.; Kim, J. C.; Ceder, G. Interface Stability in Solid-State Batteries. *Chem. Mater.* **2016**, *28*, 266–273.

(55) Billy, E.; Joulie, M.; Laucournet, R.; Boulineau, A.; DeVito, E.; Meyer, D. Dissolution Mechanisms of LiNi1/3Mn1/3Co1/3O2 Positive Electrode Material from Lithium-Ion Batteries in Acid Solution. *ACS Appl. Mater. Interfaces* **2018**, *10*, 16424–16435.

(56) Dai, T.; Zhou, H.; Liu, Y.; Cao, R.; Zhan, J.; Liu, L.; Jang, B. W.-L. Synergy of Lithium, Cobalt, and Oxygen Vacancies in Lithium Cobalt Oxide for Airborne Benzene Oxidation: A Concept of Reusing Electronic Wastes for Air Pollutant Removal. *ACS Sustainable Chem. Eng.* **2019**, *7*, 5072–5081.

(57) Towns, J.; Cockerill, T.; Dahan, M.; Foster, I.; Gaither, K.; Grimshaw, A.; Hazlewood, V.; Lanthrop, S.; Lifka, D.; Peterson, G. D.; Roskies, R.; Scott, J. R.; Wilkins-Diehr, N. XSEDE:Accelerating Scientific Discovery. *Comp. Sci. Engineering* **2014**, *16*, 62–74.